Chinese Journal of Chemical Engineering 69 (2024) 167–176

Contents lists available at ScienceDirect

Chinese Journal of Chemical Engineering

journal homepage: www.elsevier.com/locate/CJChE

Full Length Article

Particle residence time distribution and axial dispersion coefficient in a pressurized circulating fluidized bed by using multiphase particle-in-cell simulation

Jinnan Guo, Daoyin Liu*, Jiliang Ma, Cai Liang, Xiaoping Chen

Key Laboratory of Energy Thermal Conversion and Control of Ministry of Education, Southeast University, Nanjing 210096, China

A R T I C L E I N F O

Article history:
Received 8 October 2023
Received in revised form
25 January 2024
Accepted 31 January 2024
Available online 6 March 2024

Keywords:
Pressurized circulating fluidized bed
MP-PIC method
Residence time distribution
Axial dispersion coefficient

A B S T R A C T

The particle residence time distribution (RTD) and axial dispersion coefficient are key parameters for the design and operation of a pressurized circulating fluidized bed (PCFB). In this study, the effects of pressure (0.1–0.6 MPa), fluidizing gas velocity (2–7 $m\cdot s^{-1}$), and solid circulation rate (10–90 $kg\cdot m^{-2}\cdot s^{-1}$) on particle RTD and axial dispersion coefficient in a PCFB are numerically investigated based on the multiphase particle-in-cell (MP-PIC) method. The details of the gas–solid flow behaviors of PCFB are revealed. Based on the gas–solid flow pattern, the particles tend to move more orderly under elevated pressures. With an increase in either fluidizing gas velocity or solid circulation rate, the mean residence time of particles decreases while the axial dispersion coefficient increases. With an increase in pressure, the core-annulus flow is strengthened, which leads to a wider shape of the particle RTD curve and a larger mean particle residence time. The back-mixing of particles increases with increasing pressure, resulting in an increase in the axial dispersion coefficient.

1. Introduction

Circulating fluidized beds (CFBs) are widely used in industrial applications, such as fluid catalytic cracking, coal combustion, and biomass gasification, because of their excellent heat and mass transfer. In recent years, the pressurized circulating fluidized bed (PCFB) combined with oxy-fuel combustion has been proposed to improve cycle efficiency and decrease the cost of CO_2 capture [1–3]. An oxy-coal PCFB combustion cycle was analyzed [4]. With the increase in pressure, the cycle efficiency increased from 27.2% to 30.5%. Extensive studies have been conducted on combustion characteristics, operating parameters, and pollutant emissions, and quite a few merits are reported for pressurized fluidized oxy-coal combustion [5–10]. It is because an increase in pressure for bubbling fluidized beds can cause a more vigorous motion with smaller bubbles [11–13], which promotes gas-solid mixing.

With respect to an increase in pressure for circulating fluidized beds, the studies on flow dynamics are fewer. Experiment and simulation are two main methods to study the flow dynamics of a CFB operated at high pressure [14]. Extensive experimental studies have been conducted on particle concentration, particle velocity, and solid circulation rate. Richtberg *et al.* [15] studied the effect of elevated pressure on particle motion and distribution in a PCFB and found a more uniform axial and radial solid distribution with increasing pressure. Nie *et al.* [16] conducted gas–solid flow behaviors in a pressurized multi-stage circulating fluidized bed and found that the system could be more controllable under an elevated pressure and high solid circulation rate. Increasing pressure led to a higher apparent solids holdup. Feng *et al.* [17] investigated the radial profiles of particle volume fraction under various operating conditions and found that the superficial gas velocity played a more significant role than the operating pressure in particle volume fraction in the radial and axial directions. Tsukada *et al.* [18] carried out gas-solid flow experiments in a CFB under the pressure range of 0.1–0.7 MPa and found that the transition rate from bubbling to turbulent fluidization decreased with the increase in pressure, but the solid circulation rate remained almost constant under the transition rate. Further study on flow dynamics by combining experiment and simulation. Zhu *et al.* [19,20] investigated the hydrodynamic behavior of a pilot-scale PCFB at elevated pressures and found that the solid circulation rate changed from a significant

* Corresponding author.
E-mail address: dyliu@seu.edu.cn (D. Liu).

https://doi.org/10.1016/j.cjche.2024.01.020
1004-9541/

increase to slight growth with increasing operating pressure. Similarly, Dong *et al.* [14] found that increasing pressure can increase particle uniformity in the axial and radial directions. In our previous studies [21,22], gas–solid slip behaviors and the solid circulation rate at elevated pressures were correlated with operating parameters in a PCFB.

The particle residence time distribution (RTD) and axial dispersion coefficient are key parameters for the design and operation of circulating fluidized beds [23–25]. Scale-up properties of multiple-chamber fluidized beds have been explored by interpreting the residence time distribution of polydisperse particles [26]. The experimental measurement of RTD for CFB is generally based on the pulse method, including the chemical substance tracking method [27] and the radiation tracer method [28,29]. Harris *et al.* [30,31] conducted experimental measurements on RTD in a cold CFB riser and found that the fluidizing gas velocity had a significant impact on peak of particle RTD, distribution, and shape. The RTD of particles reflected the internal circulation degree of particles in the riser. Chapadgaonkar *et al.* [32] studied the RTD in a CFB through experiments and found that the mean residence time of particles decreased with an increase in the proportion of coarse particles. However, the measurement of particle RTD is time-consuming and labor-intensive. Compared with the experimental studies, the numerical simulation can directly obtain detailed information on particle motion. For instance, Luo *et al.* [33] used computational fluid dynamics-discrete element method (CFD-DEM) to simulate the full-loop gas–solid flow in a CFB, studied the particle motion characteristics from a macroscopic and microscopic perspective, and found that particles in the riser had strong back-mixing with a large distribution range of residence time. By using numerical simulation, Hua and Wang [34] systematically studied particle RTD, compared variations of mean residence time, Peclet number, and dispersion coefficient of solids under different conditions from the literature, and explained some existing contradictions in the reported effects of operating conditions on particle RTD. Shi *et al.* [35] discussed the RTD under different particle size distributions in a CFB riser using computational particle fluid dynamics (CPFD) and found that the mean residence time of particles with a wider particle size distribution was longer. Yoo *et al.* [36] used the Eulerian–Eulerian model and tracer technique to study the influence of gas jet direction on solid RTD in the riser of a CFB. The results showed that the gas jet direction had a significant effect on the axial and radial structure of the bed, which affects the RTD.

To summarize, experiments provide the most reliable results but have limitations on experimental cost and complex operating conditions [15]. The Eulerian–Eulerian model is widely used in gas–solid flow in a CFB. However, the model is not able to get particle information [37]. The CFD-DEM model can account for particle characteristics, but it takes a long time and is difficult to simulate industrial equipment [38]. Among different simulation methods for circulating fluidized beds, the multiphase particle-in-cell (MP-PIC) method is increasingly used, *e.g.* pressurized fluidized bed oxy-fuel combustion of coal [39], steam gasification of biomass [40], and CO_2 enhanced gasification of coal [41]. The special advantage of MP-PIC is that it can be applied for simulating facilities with industrial sizes and wide particle size distributions [42,43].

Through the above analysis of the existing studies, the MP-PIC method provides a strong tool for studying particle flow dynamics in CFB. However, there are limited studies on particle RTD in CFB with elevated pressures. Therefore, the current study is aimed at exploring the effects of pressure, fluidizing gas velocity, and solid circulation rate on particle RTD and axial dispersion coefficient in a full-loop PCFB by using MP-PIC simulation. The article is organized as follows: In Sections 2 and 3, the MP-PIC method is described and validated for simulating the gas–solid flow in a PCFB. In Section 4, the data analysis methods of RTD and dispersion coefficient are described. In Section 5, the results of particle movement, RTD, and axial dispersion coefficient are presented and discussed. Section 6 concludes the article.

2. Mathematic Model

2.1. Gas phase governing equation

The MP-PIC model provided by the open-source multiphase flow platform MFiX [44,45] is used, where the governing equations of the gas phase are shown below.

Continuity equation:

$$\frac{\partial(\varepsilon_g\rho_g)}{\partial t}+\nabla\cdot(\varepsilon_g\rho_g\boldsymbol{u}_g)=0 \tag{1}$$

Momentum equation:

$$\frac{\mathrm{d}}{\mathrm{d}t}(\varepsilon_g\rho_g\boldsymbol{u}_g)=\nabla\cdot\overline{\overline{S_g}}+\varepsilon_g\rho_g\boldsymbol{g}-\sum_{m=1}^{M}\boldsymbol{I}_{gm} \tag{2}$$

where $\boldsymbol{u}_g$ is the volume average gas phase velocity, ε_g is the gas volume fraction, ρ_g is the gas density, $\boldsymbol{I}_{gm}$ is the momentum exchange rate between the gas phase and solid phase, and $\boldsymbol{g}$ is the acceleration of gravity. $\overline{\overline{S_g}}$ is the force tensor:

$$\overline{\overline{S_g}}=-p_g\overline{\overline{I}}+\overline{\overline{\tau_g}} \tag{3}$$

where p_g is the gas phase pressure. $\overline{\overline{\tau_g}}$ is the gas phase shear stress tensor:

$$\overline{\overline{\tau_g}}=2\mu_g\overline{\overline{D_g}}+\lambda_g\nabla\cdot\mathrm{tr}\overline{\overline{D_g I}} \tag{4}$$

where $\overline{\overline{D_g}}=\left[\nabla\boldsymbol{u}_g+(\nabla\boldsymbol{u}_g)^{\mathrm{T}}\right]/2$ is the strain rate tensor, μ_g and λ_g are the dynamic coefficient and the second coefficient of the gas phase viscosity.

2.2. Solid phase governing equation

In the MP-PIC method [46,47], the movement of the solid phase is described by the Lagrangian approach, where the real particles are replaced by calculated particles. Each calculated particle contains n_p real particles with the same properties. When the overall characteristics of the solid phase are needed, the properties of all particles are interpolated into the fluid grid so that the solid phase has the properties of both a discrete phase and a continuous phase.

The m^{th} solid-phase is represented by N_m calculated particles. The diameter and density of each calculated particle are D_m and ρ_{sm}, respectively. For the total of M solid phases, the total number of calculated particles N is:

$$N=\sum_{m=1}^{M}N_m \tag{5}$$

The movement of the particle phase is related to the transport equation of the particle distribution function $f(\boldsymbol{x}_p,\ \boldsymbol{u}_p,\ m_p,\ t)$. Therefore, $f(\boldsymbol{x}_p,\boldsymbol{u}_p,m_p,t)\mathrm{d}m_p\mathrm{d}\boldsymbol{u}_p$ is the particle distribution function in a specific mass interval, velocity and position at time t. The transport equation corresponding to the particle distribution function is as follows:

$$\frac{\partial f}{\partial t}+\nabla\boldsymbol{\cdot}(f\boldsymbol{u}_{\mathrm{p}})+\nabla u_p\boldsymbol{\cdot}\left(\frac{\mathrm{d}\boldsymbol{u}_{\mathrm{p}}}{\mathrm{d}t}f\right)=\frac{f_{\mathrm{D}}-f}{\tau_{\mathrm{D}}}+\frac{f_{\mathrm{G}}-f}{\tau_{\mathrm{G}}} \tag{6}$$

where f_D is the distribution function of particles in the local equilibrium state, τ_D is the relaxation time of collision between particles, f_G is the distribution function of the particles in the local equilibrium state under the Gaussian distribution effect, and τ_G is the relaxation time of particle collisions under the Gaussian distribution effect.

For the dynamic information of i^{th} particle, the relevant calculation equations for its displacement and velocity are as follows:

$$\frac{\mathrm{d}\boldsymbol{x}_{\mathrm{p}}(t)}{\mathrm{d}t}=\boldsymbol{u}_{\mathrm{p}}(t) \tag{7}$$

$$m_{\mathrm{p}}\frac{\mathrm{d}\boldsymbol{u}_{\mathrm{p}}(t)}{\mathrm{d}t}=m_{\mathrm{p}}\boldsymbol{g}+\boldsymbol{F}_{\mathrm{p,drag}}(t)+\boldsymbol{F}_{\mathrm{p,coll}}(t) \tag{8}$$

where $\boldsymbol{F}_{\mathrm{p,drag}}(t)$ is the drag force acting on particles, and $\boldsymbol{F}_{\mathrm{p,coll}}(t)$ is the force generated by collision between particles.

2.3. Gas–solid interaction: drag force model

The drag force determines the momentum transfer between two phases, which affects the movement and distribution of particles. In this study, the Gidaspow drag force model [48] is used, and the corresponding equation is as follows:

$$\beta_{\mathrm{p}}=\begin{cases}\dfrac{3}{4}C_{\mathrm{D}}\dfrac{\rho_{\mathrm{g}}\varepsilon_{\mathrm{s}}\varepsilon_{\mathrm{g}}|\boldsymbol{u}_{\mathrm{g}}-\boldsymbol{u}_{\mathrm{p}}|}{d_{\mathrm{p}}}\varepsilon_{\mathrm{g}}{}^{-2.65}, & \varepsilon_{\mathrm{g}}\geq 0.8\\ \dfrac{150\varepsilon_{\mathrm{s}}(1-\varepsilon_{\mathrm{g}})\mu_{\mathrm{g}}|\boldsymbol{u}_{\mathrm{g}}-\boldsymbol{u}_{\mathrm{p}}|}{\varepsilon_{\mathrm{g}}d_{\mathrm{p}}{}^{2}(1-\varepsilon_{\mathrm{g}})}+\dfrac{1.75\rho_{\mathrm{g}}\varepsilon_{\mathrm{s}}|\boldsymbol{u}_{\mathrm{g}}-\boldsymbol{u}_{\mathrm{p}}|}{d_{\mathrm{p}}}, & \varepsilon_{\mathrm{g}}<0.8\end{cases} \tag{9}$$

$$C_{\mathrm{D}}=\begin{cases}\dfrac{24}{Re_{\mathrm{P}}\left(1+0.15Re_{\mathrm{P}}{}^{0.687}\right)}, & Re_{\mathrm{P}}<1000\\ 0.44, & Re_{\mathrm{P}}\geq 1000\end{cases} \tag{10}$$

$$Re_{\mathrm{P}}=\frac{\rho_{\mathrm{g}}\varepsilon_{\mathrm{g}}|\boldsymbol{u}_{\mathrm{g}}-\boldsymbol{u}_{\mathrm{p}}|d_{\mathrm{p}}}{\mu_{\mathrm{g}}} \tag{11}$$

where d_p is particle diameter, ε_s is average particle volume fraction.

2.4. Particle–particle interaction: solid collision

The collision between particles is described by a hard-sphere model based on the law of momentum conservation. The friction coefficient and restitution coefficient are used to calculate particle velocity after collision. It is assumed that the particle collision process is completed within a time step. The MP-PIC method does not directly solve the collision of each particle but solves the stress gradient of the particle in the Eulerian grid and then assigns the value to the particle at the corresponding position by interpolation to simulate particle collisions. The force $\boldsymbol{F}_{\mathrm{p,coll}}$ produced by collisions between particles is as follows:

$$\boldsymbol{F}_{\mathrm{p,coll}}=-\frac{\boldsymbol{u}_{\mathrm{p}}}{\varepsilon_{\mathrm{s}}}\nabla\tau_{\mathrm{p}} \tag{12}$$

where τ_p is the particle normal stress, which is calculated by Harris and Crighton's model [49]:

$$\tau_{\mathrm{p}}=\frac{p_{\mathrm{s}}\varepsilon_{\mathrm{s}}^{\beta}}{\max\left[\varepsilon_{\mathrm{b}}-\varepsilon_{\mathrm{s},}\theta(1-\varepsilon_{\mathrm{s}})\right]} \tag{13}$$

where p_s is a constant, which is usually between 1 Pa and 100 Pa. The ε_b is the maximum allowable particle volume fraction, β is constant, which takes a value of 2–5, and θ is constant, which takes a value of 10^{-7} [50].

2.5. Wall boundary conditions

In the model, the gas phase uses the nonslip boundary wall condition. The collision between a particle and wall uses inelastic collision:

$$\boldsymbol{n}\cdot\boldsymbol{u}_{\mathrm{p}}=-e_{\mathrm{wn}}\boldsymbol{n}\cdot\boldsymbol{u}_{\mathrm{p}}^{(0)} \tag{14}$$

$$\boldsymbol{\tau}\cdot\boldsymbol{u}_{\mathrm{p}}=-e_{\mathrm{w}\tau}\boldsymbol{\tau}\cdot\boldsymbol{u}_{\mathrm{p}}^{(0)} \tag{15}$$

where e_{wn} and $e_{w\tau}$ are the normal and tangential collision restitution coefficients during the collision between the particle and wall, respectively.

The velocities of the fluidizing gas and the aeration gas in the loop-seal are specified at the inlets. The outlet is the pressure outlet boundary. Initially, the solid phase is uniformly distributed in the returner and downcomer according to the specified volume fraction. The initial velocities of the gas phase and the solid phase are both set to zero.

3. Simulation Conditions

3.1. Experimental setup

Fig. 1 shows the circulating fluidized bed, which is mainly composed of a riser, cyclone, downcomer, and loop seal. A full-loop PCFB is studied. Compared with the periodic boundary condition, adding a full-loop PCFB ensures the stability of the simulation, which more closely matches the actual circumstances. The details can be referred to in our previous study [22]. Here, a brief description is presented. Both the inner diameter of the riser and the dipleg are 0.05 m. The height of the riser is 3.3 m with an L-type exit. Air is used as the fluidizing agent and is introduced from the bottom distributor. The recirculation inlet of the solid is located 420 mm above the distributor. The sand is used as bed material, which has a density of 2550 $\mathrm{kg\cdot m^{-3}}$ and an average particle size d_p of 537 μm.

3.2. Numerical validation

The three-dimensional geometric model is constructed using the stereolithography (STL) format file. The cut-cell grid is used to mesh the complex geometry. The minimum grid sizes in the three directions of *X*, *Y* and *Z* are 8.6, 7.2 and 4.5 mm, which is about 15 times the particle size.

In order to validate the accuracy of the model, a condition with a pressure of 0.3 MPa and a fluidizing gas velocity of 3 $\mathrm{m\cdot s^{-1}}$ is used for comparison. The particle properties and main numerical parameters related to the simulation are listed in Table 1. By simulating this case for 80 s, the time average of parameters during 60–80 s is calculated and compared with experimental values.

It should be pointed out that the sensitivity analysis of key parameters in the MP-PIC model, such as the normal collision coefficient of restitution e_{wn}, tangent collision coefficient of restitution $e_{w\tau}$, number of real particles per computational particle n_p, were considered when testing the model. Regarding the collision between particle and wall, Wu *et al.* [51] compared the particle collision coefficient of restitution from 0.5 to 0.95 and found that the values of each parameter were very close. For the number of real particles per computational particle, Nikolopoulos *et al.* [52] found that it had a limited effect on the pressure distribution of the bed. Ostermeier *et al.* [53] found that the MP-PIC model was more dependent on the mesh size than on the number of real particles per calculated particle.

Fig. 2 shows the comparison of simulation results and experimental data. As shown in Fig. 2(a), the predicted particle volume fraction agrees reasonably with the experimental data along the axial direction by using the Gidaspow drag model, especially in the dilute region and transition region. While there is a slight difference between simulation results and experimental data in the dense region, which is the nonuniform gas–solid flow. The solid circulation rate obtained from the simulation using the Gidaspow drag model fluctuates near a fixed value of 23.3 $kg \cdot m^{-2} \cdot s^{-1}$, which is consistent with the experimental data of 21.47 $kg \cdot m^{-2} \cdot s^{-1}$ under the same operating conditions. Thus, the MP-PIC method is reasonable to simulate the solid circulation rate in a pressurized circulating fluidized bed by using the Gidaspow drag model.

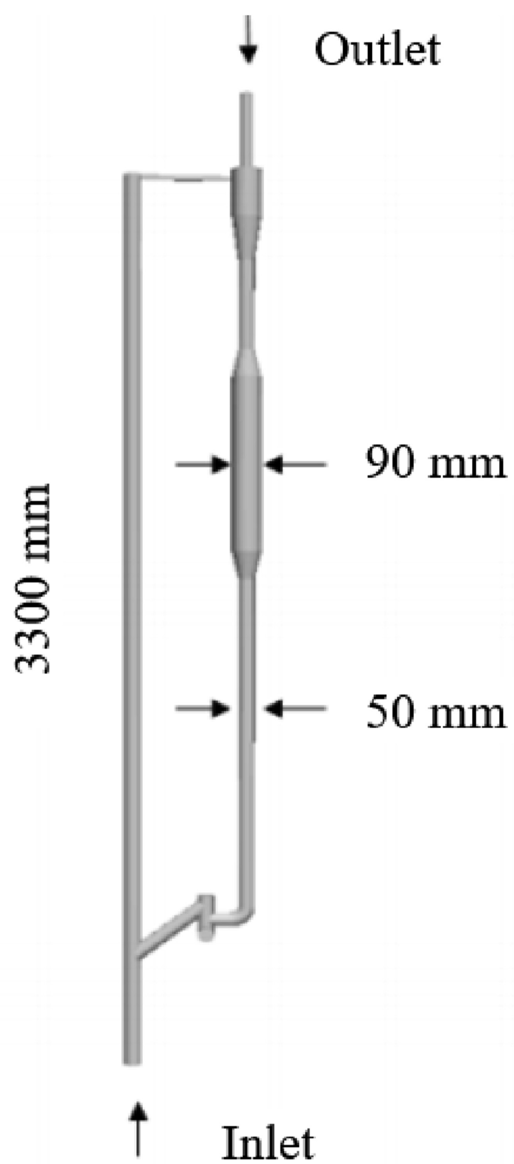

Fig. 1. Simplified model of the CFB system.

3.3. Test conditions

The operation is at room temperature, while the pressures are 0.1, 0.3 and 0.6 MPa, and the corresponding gas densities are 1.18, 3.51 and 7.01 $kg \cdot m^{-3}$, respectively. For different pressures, the fluidizing gas velocity varies from 2 to 7 $m \cdot s^{-1}$. The minimum fluidizing gas velocity for the used particles under 0.1, 0.3 and 0.6 MPa is 0.209, 0.145 and 0.128 $m \cdot s^{-1}$, respectively, which were reported in our previous study [54].

4. Data Analysis Method

4.1. Axial and radial distribution of particle volume fraction

A list of eight points is monitored along the axial direction of the riser. The vertical heights between the monitoring points and the air distributor are 250, 380, 720, 1170, 1690, 2440, 3040 and 3270 mm, respectively. In the horizontal plane, the above eight points are monitored for particle volume fraction. The ratios of r to the riser radius R are 0, 0.2, 0.4, 0.6, 0.8 and 0.98. In the process of data extraction, statistical analysis is performed on the particle volume fraction of each monitoring point.

4.2. Solid circulation rate

Solid circulation rate refers to the particle mass flow rate per unit cross section, which is changed by changing the fluidizing gas velocity. A monitoring surface at the outlet of the riser is set at 3270 mm from the vertical height of the air distribution plate to calculate the particle mass flow rate q_m. Then, the particle mass flow rate is converted to the solid circulation rate (G_s):

$$G_s = \frac{q_m}{A_R} \tag{16}$$

where A_R is the cross-sectional area of the riser.

4.3. Particle residence time distribution

When calculating particle residence time distribution (RTD) in the riser, two monitoring surfaces at the inlet and outlet of the riser are set. Each time the particles pass through the monitoring surface, the corresponding time difference is the residence time of the particles in the riser.

Table 1
Simulation parameters used in MP-PIC model

Parameter	Value
Gas density/$kg \cdot m^{-3}$	3.51
Gas viscosity/$kg \cdot m^{-1} \cdot s^{-1}$	1.7×10^{-5}
Particle diameter/μm	537
Particle density/$kg \cdot m^{-3}$	2500
Particle packing density/$kg \cdot m^{-3}$	0.6
Number of numerical calculated particle	219116
Number of real particles per calculated particle	200
Number of real particles	4.4×10^7
Empirical dampening factor	0.85
Normal collision coefficient of restitution	0.85
Tangent collision coefficient of restitution	0.85
Time step/s	1×10^{-4}
Physical simulation time/s	80
Save frequency/Hz	50

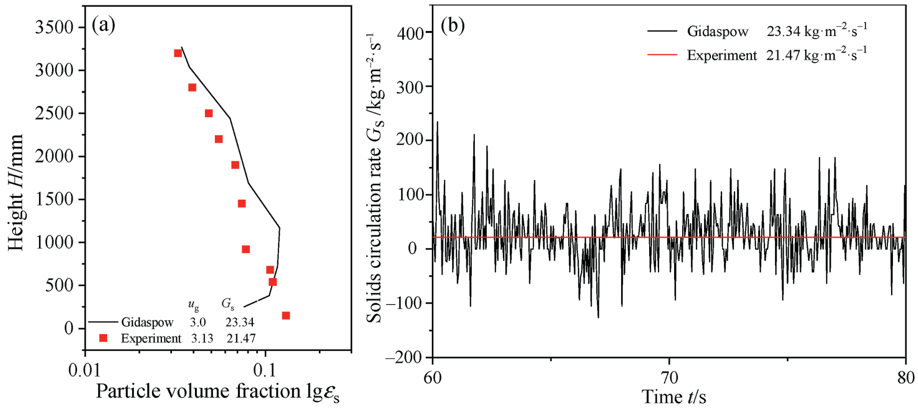

Fig. 2. Comparison of the simulation results and experimental data [16] (a) axial particle volume fraction along the riser; (b) solid circulation rate over time.

Usually, the particle residence time distribution is plotted in the form of a probability distribution graph (E-curve) [55]. Through normalization, the E-curve satisfies the requirement of $\int_0^\infty E(t)\mathrm{d}t = 1$, which can be described by mean and variance as follows:

$$t_{\text{mean}} = \int_0^\infty tE(t)\mathrm{d}t \tag{17}$$

where t_{mean} represents the average value of the residence time of all particles in the component.

4.4. Particle axial dispersion coefficient

The method for calculating the axial dispersion coefficient of particles is based on the trajectory of a single particle [33,55]. In this study, all of the calculated particles, that is, 219116, are used to calculate the particle axial dispersion coefficient. If a number of N particles are injected at (x_0, y_0, z_0) when $t = 0$, the instantaneous displacement of each particle can be expressed as:

$$Y = y(t) - y_0 \tag{18}$$

The average axial displacement of tracer particles at time t is:

$$\overline{Y} = \frac{1}{N}\sum_{n=1}^{N} y_n \tag{19}$$

The variance of the particle's axial displacement at time t is:

$$\overline{Y}^2 = \frac{1}{N}\sum_{i=1}^{N}(y_i - \overline{Y})^2 \tag{20}$$

The particle axial dispersion coefficient (Da) can be expressed as:

$$D_a = \frac{\mathrm{d}\overline{Y}^2}{2\mathrm{d}t} \tag{21}$$

In the momentum and mass transfer of gas–solid flow, the

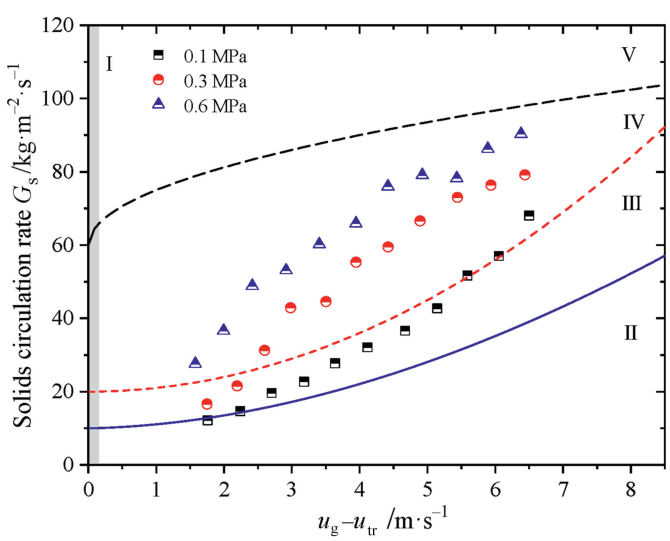

Fig. 3. Gas–solid flow diagram under different simulated working conditions (region II: DRF, region III: CAF, region IV: CAF + TFBB, region V: DRU).

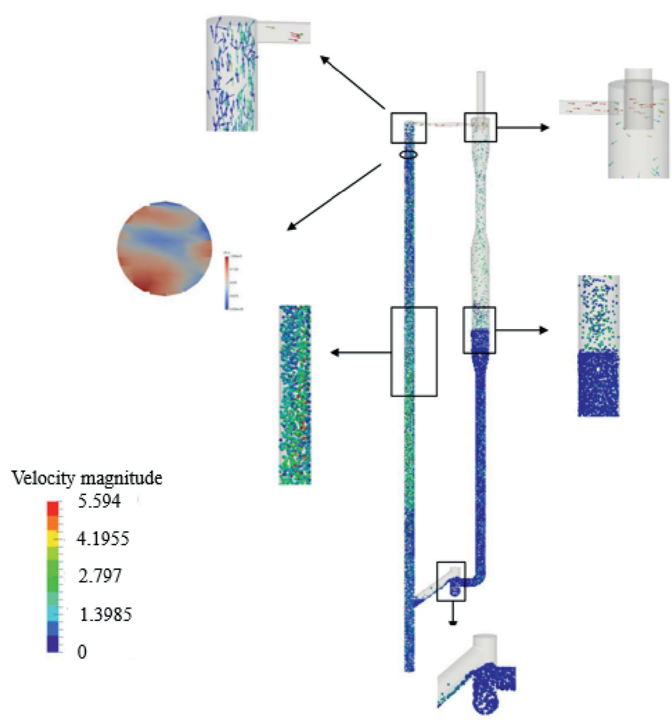

Fig. 4. Details of gas–solid flow behavior of PCFB.

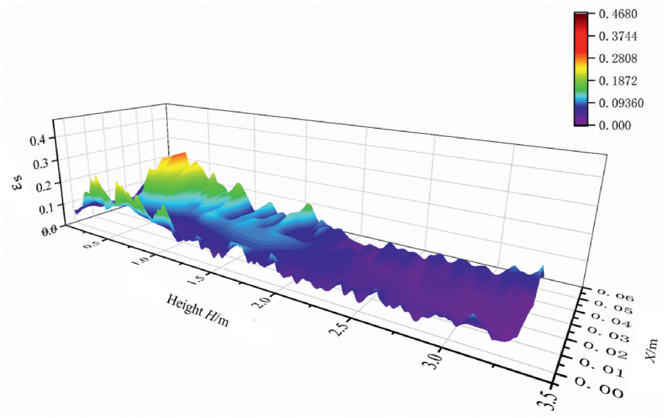

Fig. 5. 3D surface plots of particle volume fraction of longitudinal section of riser.

Peclet number, Pe, is used to describe the relative magnitude of convection and dispersion:

$$Pe = \frac{uL}{D} \tag{22}$$

where u is particle convection velocity, L is the displacement during particle movement, and D is the particle dispersion coefficient.

The estimation equation of particle convection velocity u is $L/\bar{t}$, where L corresponds to the net height of the riser and $\bar{t}$ is particle mean residence time. For numerical simulation, $\bar{t}$ is taken as t_{mean}. Therefore, the calculation equation for the Peclet number corresponding to the axial particle dispersion in the riser is:

$$Pe_{\text{a}} = \frac{L^2}{t_{\text{mean}} D_{\text{a}}} \tag{23}$$

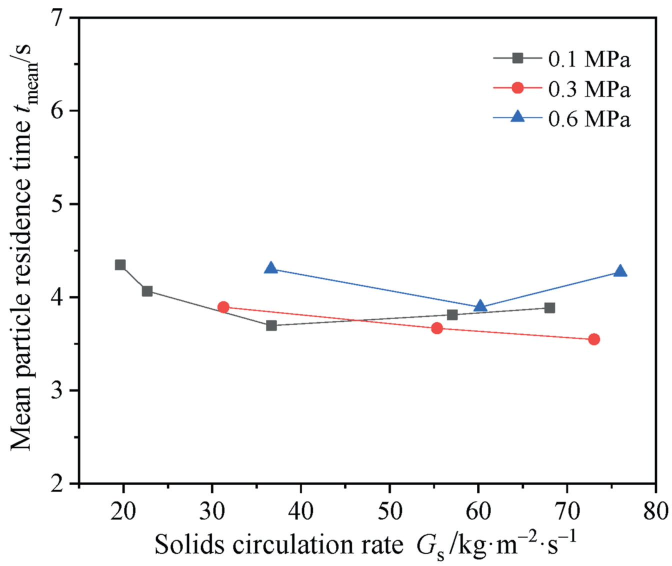

Fig. 7. Mean particle residence time under different solid circulation rate.

5. Results and Discussion

5.1. Gas–solid flow diagram

A gas–solid flow diagram is proposed for the purpose of a better comprehension of the hydrodynamic characters and a better definition of the design and operation parameters [56–58]. Fig. 3 shows the gas–solid flow diagram under different simulated working conditions [58]. In terms of $u_{\text{g}} - u_{\text{tr}}$ and G_{s}, the operation regimes in the riser of a CFB are divided into the following regimes:

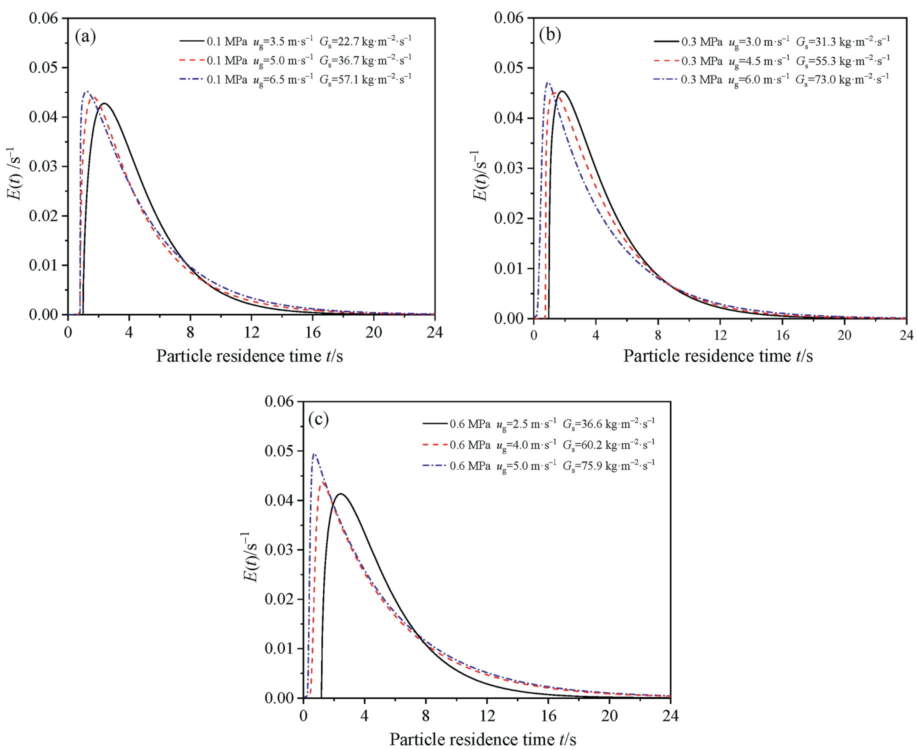

Fig. 6. Effects of solid circulation rate on RTD: (a) p = 0.1 MPa; (b) p = 0.3 MPa; (c) p = 0.6 MPa.

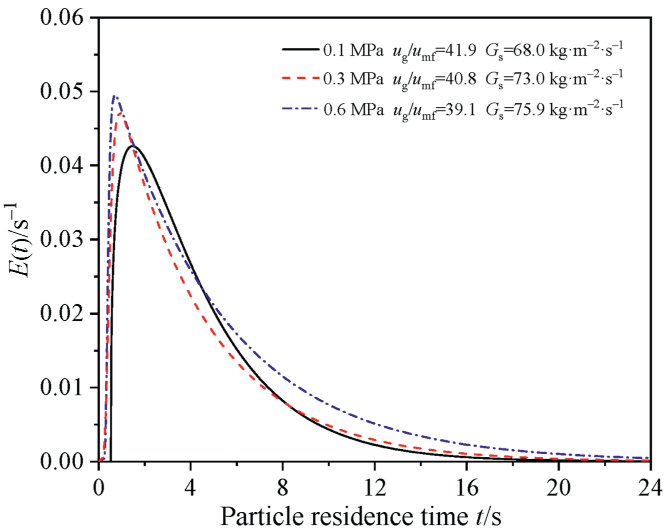

Fig. 8. Effects of pressure on particle residence time distribution.

dilute riser flow (DRF), core-annulus flow (CAF), CAF with turbulent fluidized bed at the bottom (TFBB), and dense riser upflow (DRU). In this study, the majority of simulation results are in the flow modes of CAF only and core-annulus flow with TFBB. This diagram can be helpful for CFB design using the combined ($u_{\rm g} - u_{\rm tr}, G_{\rm s}$) values.

5.2. Full-loop characteristics of pressurized circulating fluidized bed

Fig. 4 shows the details of gas–solid flow behavior. Particles in the dense region are blown up by fluidizing gas from the bottom distributor and accelerated in the low part of the riser. After this, the particle velocity gradually decreases in the dilute region and the transition region. Then, the gas–solid mixture flows into the cyclone separator. The gas flows out from the central tube of the cyclone separator, and the particles flow out from the lower exit of the cyclone separator. The falling particles pass through the solids return leg and are sent into the riser by the gas flow in the loop-seal for continuous circulation.

Fig. 5 shows 3D surface plots of the particle volume fraction of the riser. It is seen that the particle volume fraction is unevenly distributed and decreases gradually along the axial direction of the riser. The CAF structure is also observed along the whole riser. Generally, the particle volume fraction in the center of the bed is lower (less than 0.05), while the particle volume fraction at the wall is larger (more than 0.1). Besides, the CAF is also greatly changed along the bed height, with the annulus region diminishing and the core region extending to the vicinity of the riser wall.

5.3. Particle residence time

Fig. 6 shows the particle RTD under different fluidizing gas velocities and solid circulation rates. It can be seen that with the increase in fluidizing gas velocity and solid circulation rate, the starting time of the particle RTD curve has a decreasing trend. It is because with the increase in fluidizing gas velocity and solid circulation rate, the average velocity of particles increases, causing an earlier peak time, a larger peak, and a sharp-shaped residence time distribution. It can also be observed that as the fluidizing gas velocity and solid circulation rate increase, the width of the distribution increases. The increase in fluidizing gas velocity causes a decrease in the tail. However, the increase in solid circulation rate means an increase in the particle volume fraction, which reflects the increase in the particle back-mixing and in turn leads to an increase in the width of the distribution [34].

Fig. 7 shows the particle mean residence time in the riser under different solid circulation rates. Under the same pressure, the mean residence time tends to decrease slightly with the increase in solid circulation rate. With the increase in solid circulation rate, the

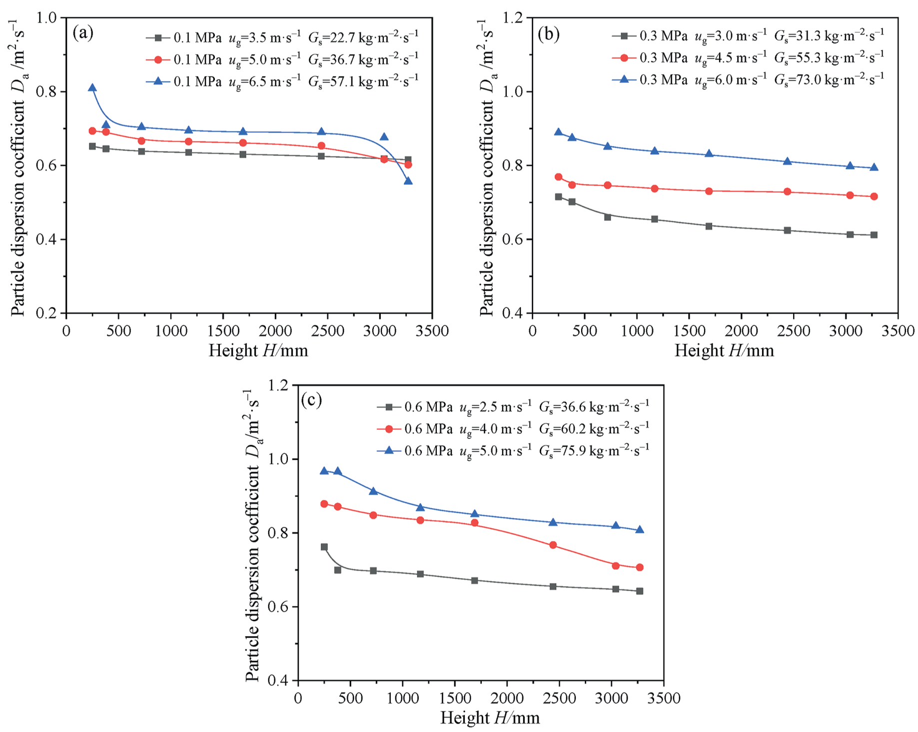

Fig. 9. Axial dispersion coefficients along the bed height under different solid circulation rate: (a) p = 0.1 MPa; (b) p = 0.3 MPa; (c) p = 0.6 MPa.

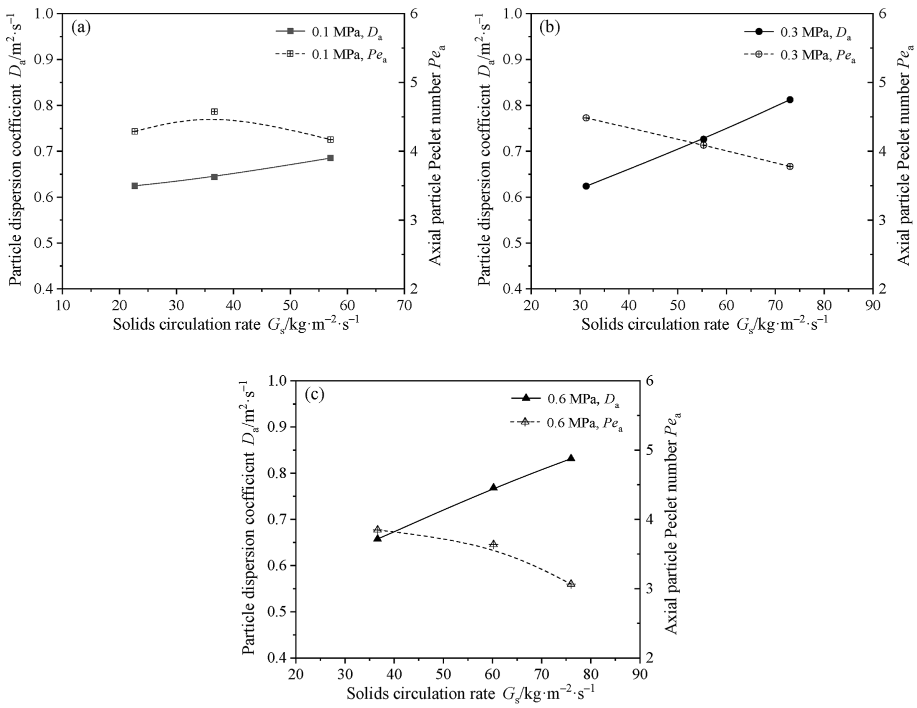

Fig. 10. Effects of solid circulation rate on axial dispersion coefficient and axial Peclet number: (a) p = 0.1 MPa; (b) p = 0.3 MPa; (c) p = 0.6 MPa.

particle volume fraction increases in the riser, leading to a slight increase in particle mean residence time.

The cases with the same fluidization number u_g/u_{mf} and solid circulation rate under different pressures are selected for analysis, as shown in Fig. 8. When the fluidization number and solid circulation rate are the same, the RTD curve becomes wider and the tail increases with the increase in pressure, indicating an increase in back-mixing and enhanced CAF structure.

5.4. Particle axial dispersion coefficient

The cases of different solid circulation rates under the same pressure are shown in Fig. 9. It can be seen that the axial dispersion coefficient shows a decreasing trend along the bed height.

Fig. 10 shows that with an increase in fluidizing gas velocity and solid circulation rate, the axial dispersion coefficient increases. As the solid circulation rate increases, the internal circulation of particles increases, which leads to an increase in the axial diffusion coefficient and a decrease in the axial Peclet number.

The cases with different pressures under the same solid circulation rate and fluidization number are shown in Fig. 11. The axial dispersion coefficient under different conditions shows a decreasing trend with an increase in bed height. Fig. 12 shows the effect of pressure on the particle axial dispersion coefficient and axial Peclet number. With the increase in pressure, the axial dispersion coefficient increases and the axial Peclet number decreases. This is because when pressure increases, the CAF structure is strengthened and the back-mixing of particles increases, resulting in an increase in the axial dispersion coefficient.

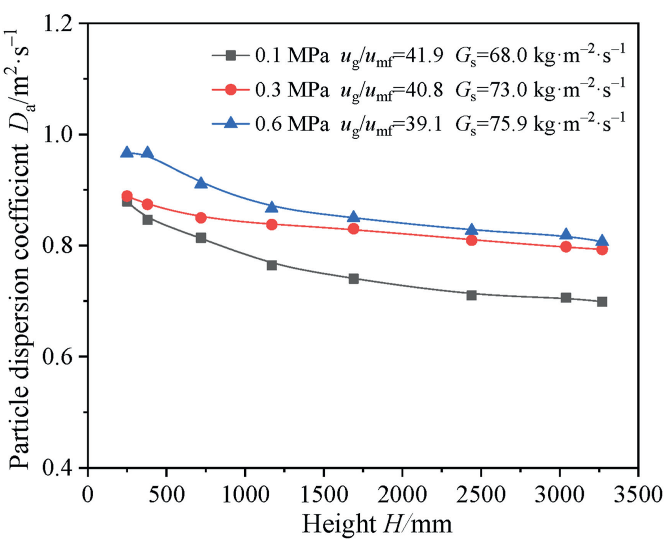

Fig. 11. Axial dispersion coefficient along the bed height under different pressures.

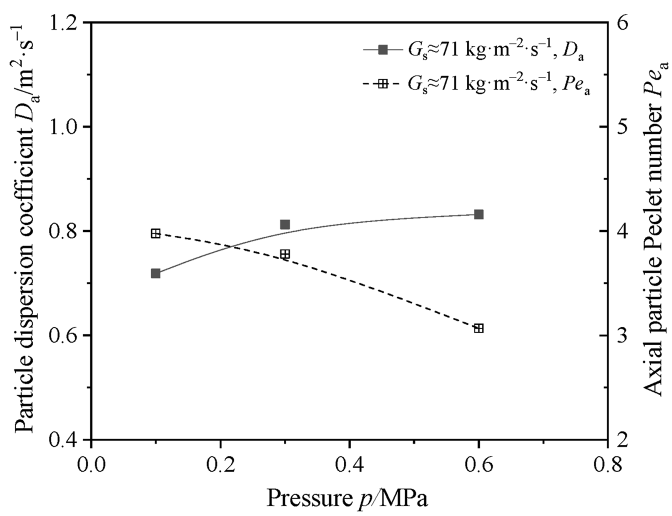

Fig. 12. Effects of pressure on the axial dispersion coefficient and the axial Peclet number.

6. Conclusions

The distribution of particle residence time and axial dispersion coefficient of pressurized circulating fluidized bed is studied by simulation using the MP-PIC model. The main conclusions are listed as follows:

(1) The CAF structure is observed in the riser. Along the riser height, the annulus region diminishes, and the core region extends to the vicinity of the riser wall. Compared with conditions in the atmosphere, the axial particle volume fraction distribution under pressurized conditions is more uniform.
(2) By increasing the fluidizing gas velocity or solid circulation rate, the particle mean residence time decreases. With increasing pressure, the core-annulus flow is strengthened, which leads to a wider shape of the particle residence time distribution curve.
(3) As the fluidizing gas velocity increases, the axial dispersion coefficient increases, and the axial Peclet number decreases. By increasing the solid circulation rate, the internal circulation of particles increases, which leads to an increase in the axial dispersion coefficient and a decrease in the axial Peclet number. By increasing pressure, the back-mixing of particles increases, resulting in an increase in the axial dispersion coefficient.

Declaration of Interest

The authors declare that they have no known competing financial interests or personal relationships that could have appeared to influence the work reported in this paper.

Acknowledgements

Financial support of this work by National Natural Science Foundation of China (51976037) is gratefully acknowledged.

References

[1] J. Hong, G. Chaudhry, J.G. Brisson, R. Field, M. Gazzino, A.F. Ghoniem, Analysis of oxy-fuel combustion power cycle utilizing a pressurized coal combustor, *Energy* 34 (9) (2009) 1332–1340.
[2] E.S. Rubin, H. Mantripragada, A. Marks, P. Versteeg, J. Kitchin, The outlook for improved carbon capture technology, *Prog. Energy Combust. Sci.* 38 (5) (2012) 630–671.
[3] S. Yadav, S.S. Mondal, A review on the progress and prospects of oxy-fuel carbon capture and sequestration (CCS) technology, *Fuel* 308 (2022) 122057.
[4] Y. Shi, W.Q. Zhong, Y.J. Shao, X.J. Liu, Energy efficiency analysis of pressurized oxy-coal combustion system utilizing circulating fluidized bed, *Appl. Therm. Eng.* 150 (2019) 1104–1115.
[5] Y.Q. Duan, L.B. Duan, J. Wang, E.J. Anthony, Observation of simultaneously low CO, NO_x and SO_2 emission during oxy-coal combustion in a pressurized fluidized bed, *Fuel* 242 (2019) 374–381.
[6] L. Li, L.B. Duan, Z.H. Yang, C.S. Zhao, Pressurized oxy-fuel combustion characteristics of single coal particle in a visualized fluidized bed combustor, *Combust. Flame* 211 (2020) 218–228.
[7] Q.W. Liu, W.Q. Zhong, A.B. Yu, C.H. Wang, Co-firing of coal and biomass under pressurized oxy-fuel combustion mode in a 10 kW_{th} fluidized bed: Nitrogen and sulfur pollutants, *Chem. Eng. J.* 450 (2022) 138401.
[8] L. Pang, Y.J. Shao, W.Q. Zhong, H. Liu, Experimental investigation on the coal combustion in a pressurized fluidized bed, *Energy* 165 (2018) 1119–1128.
[9] D. Stokie, P. Verma, B.M. Kumfer, G. Yablonsky, A.K. Suresh, R.L. Axelbaum, Pilot-scale testing of direct contact cooler for the removal of SO_x and NO_x from the flue gas of pressurized oxy-coal combustion, *Chem. Eng. J.* 414 (2021) 128757.
[10] M. Vodička, N.E. Haugen, A. Gruber, J. Hrdlička, NO_x formation in oxy-fuel combustion of lignite in a bubbling fluidized bed – Modelling and experimental verification, *Int. J. Greenh. Gas Contr.* 76 (2018) 208–214.
[11] D.Y. Liu, J.L. Song, J.L. Ma, X.P. Chen, B. van Wachem, Gas flow distribution and solid dynamics in a thin rectangular pressurized fluidized bed using CFD-DEM simulation, *Powder Technol.* 373 (2020) 369–383.
[12] I. Sidorenko, M.J. Rhodes, Influence of pressure on fluidization properties, *Powder Technol.* 141 (1–2) (2004) 137–154.
[13] X.L. Zhu, Y.B. Liu, Y.H. Li, H.G. Wang, Z.B. Wang, Bubble behaviors of Geldart B particle in a pseudo two-dimensional pressurized fluidized bed, *Particuology* 79 (2023) 121–132.
[14] P.F. Dong, Q.Y. Tu, H.G. Wang, Z.P. Zhu, Effects of pressure on flow characteristics in a pressurized circulating fluidized bed, *Particuology* 59 (2021) 16–23.
[15] M. Richtberg, R. Richter, K.E. Wirth, Characterization of the flow patterns in a pressurized circulating fluidized bed, *Powder Technol.* 155 (2) (2005) 145–152.
[16] W. Nie, R.T. Feng, J.G. Li, Z.H. Hao, H.J. Zhan, Z.H. Cheng, Y.T. Fang, Gas–solid flow behaviors in a pressurized multi-stage circulating fluidized bed with Geldart group B particles, *Int. J. Chem. React. Eng.* 17 (12) (2019) 20190087.
[17] R.T. Feng, J.G. Li, L.B. Dong, Z.H. Hao, Z.R. Ba, H.J. Zhan, Y.T. Fang, Gas–solid flow behaviors in a multi-stage circulating fluidized bed under elevated pressure, *Chem. Eng. Sci.* 196 (2019) 1–13.
[18] M. Tsukada, D. Nakanishi, M. Horio, The effect of pressure on the phase transition from bubbling to turbulent fluidization, *Int. J. Multiph. Flow* 19 (1) (1993) 27–34.
[19] X.L. Zhu, P.F. Dong, Q.Y. Tu, Z.P. Zhu, W.Q. Yang, H.G. Wang, Investigation of gas–solids flow characteristics in a pressurised circulating fluidised bed by experiment and simulation, *Powder Technol.* 366 (2020) 420–433.
[20] X.L. Zhu, P.F. Dong, Q.Y. Tu, Z.P. Zhu, W.Q. Yang, H.G. Wang, Investigation of gas–solid flow characteristics in the cyclone dipleg of a pressurised circulating fluidised bed by ECT measurement and CPFD simulation, *Meas. Sci. Technol.* 30 (5) (2019) 054002.
[21] J.D. Hu, D.Y. Liu, H. Li, C. Liang, X.P. Chen, Experimental study of the solid circulation rate in a pressurized circulating fluidized bed, *Particuology* 56 (2021) 207–214.
[22] D.Y. Liu, J.D. Hu, J.L. Song, C. Liang, C.L. Xu, X.P. Chen, Effect of elevated pressure on gas–solid flow characteristics in a circulating fluidized bed, *Powder Technol.* 366 (2020) 470–476.
[23] Y.J. Gao, F.J. Muzzio, M.G. Ierapetritou, A review of the residence time distribution (RTD) applications in solid unit operations, *Powder Technol.* 228 (2012) 416–423.
[24] S. Mahmoudi, J.P.K. Seville, J. Baeyens, The residence time distribution and mixing of the gas phase in the riser of a circulating fluidized bed, *Powder Technol.* 203 (2) (2010) 322–330.
[25] J.W. Zhang, G.W. Xu, Scale-up of bubbling fluidized beds with continuous particle flow based on particle-residence-time distribution, *Particuology* 19 (2015) 155–163.
[26] B. Lan, J. Xu, P. Zhao, Z. Zou, J.W. Wang, Q.S. Zhu, Scale-up effect of residence time distribution of polydisperse particles in continuously operated multiple-chamber fluidized beds, *Chem. Eng. Sci.* 244 (2021) 116809.
[27] M.J. Rhodes, S. Zhou, T. Hirama, H. Cheng, Effects of operating conditions on longitudinal solids mixing in a circulating fluidized bed riser, *AIChE J.* 37 (10) (1991) 1450–1458.
[28] C.W. Chan, J. Seville, Z.F. Yang, J. Baeyens, Particle motion in the CFB riser with special emphasis on PEPT-imaging of the bottom section, *Powder Technol.* 196 (3) (2009) 318–325.
[29] M. Van de Velden, J. Baeyens, J.P.K. Seville, X. Fan, The solids flow in the riser of a circulating fluidised bed (CFB) viewed by positron emission particle tracking (PEPT), *Powder Technol.* 183 (2) (2008) 290–296.
[30] A.T. Harris, J.F. Davidson, R.B. Thorpe, A novel method for measuring the residence time distribution in short time scale particulate systems, *Chem. Eng. J.* 89 (1–3) (2002) 127–142.
[31] A.T. Harris, J.F. Davidson, R.B. Thorpe, Particle residence time distributions in circulating fluidised beds, *Chem. Eng. Sci.* 58 (11) (2003) 2181–2202.
[32] S.S. Chapadgaonkar, Y.P. Setty, Residence time distribution of solids in a fluidised bed, *Indian J. Chem. Technol.* 6 (1999) 100–106.
[33] K. Luo, F. Wu, S.L. Yang, M.M. Fang, J.R. Fan, High-fidelity simulation of the 3-D full-loop gas–solid flow characteristics in the circulating fluidized bed, *Chem. Eng. Sci.* 123 (2015) 22–38.
[34] L.N. Hua, J.W. Wang, Residence time distribution of particles in circulating fluidized bed risers, *Chem. Eng. Sci.* 186 (2018) 168–190.
[35] X.G. Shi, X.Y. Lan, F. Liu, Y.H. Zhang, J.S. Gao, Effect of particle size distribution on hydrodynamics and solids back-mixing in CFB risers using CPFD simulation, *Powder Technol.* 266 (2014) 135–143.
[36] H. Yoo, H. Moon, S. Choi, Y.K. Park, H.H. Cho, Effect of the jet direction of gas nozzle on the residence time distribution of solids in circulating fluidized bed risers, *J. Taiwan Inst. Chem. Eng.* 71 (2017) 235–243.
[37] Q. Zhou, J.W. Wang, J.H. Li, Three-dimensional simulation of dense suspension upflow regime in high-density CFB risers with EMMS-based two-fluid model, *Chem. Eng. Sci.* 107 (2014) 206–217.
[38] D.M. Snider, S.M. Clark, P.J. O'Rourke, Eulerian–Lagrangian method for three-dimensional thermal reacting flow with application to coal gasifiers, *Chem. Eng. Sci.* 66 (6) (2011) 1285–1295.
[39] J.R. Gu, Y.J. Shao, W.Q. Zhong, 3D simulation on pressurized oxy-fuel combustion of coal in fluidized bed, *Adv. Powder Technol.* 31 (7) (2020) 2792–2805.
[40] S.L. Yang, F.H. Fan, Y.G. Wei, J.H. Hu, H. Wang, S.H. Wu, Three-dimensional MP-PIC simulation of the steam gasification of biomass in a spouted bed gasifier, *Energy Convers. Manag.* 210 (2020) 112689.

[41] A. Klimanek, J. Bigda, CFD modelling of CO_2 enhanced gasification of coal in a pressurized circulating fluidized bed reactor, *Energy* 160 (2018) 710−719.
[42] X.H. Liu, S. Wang, S.L. Yang, H. Wang, Investigation of cluster property in the riser of circulating fluidized bed with a wide particle size distribution, *Powder Technol.* 390 (2021) 273−291.
[43] S.L. Yang, S. Wang, H. Wang, Impact of polydispersity on the flow dynamics in the riser of a circulating fluidized bed, *Powder Technol.* 381 (2021) 489−502.
[44] C. Li, Q. Eri, Comparison between two Eulerian−Lagrangian methods: CFD-DEM and MPPIC on the biomass gasification in a fluidized bed, *Biomass Convers. Bioresour.* 13 (2023) 3819−3836.
[45] A. Vaidheeswaran, A. Gel, M.A. Clarke, W.A. Rogers, Assessment of model parameters in MFiX particle-in-cell approach, *Adv. Powder Technol.* 32 (8) (2021) 2962−2977.
[46] M.J. Andrews, P.J. O'Rourke, The multiphase particle-in-cell (MP-PIC) method for dense particulate flows, *Int. J. Multiph. Flow* 22 (2) (1996) 379−402.
[47] D.M. Snider, An incompressible three-dimensional multiphase particle-in-cell model for dense particle flows, *J. Comput. Phys.* 170 (2) (2001) 523−549.
[48] D. Gidaspow, J. Jung, R.K. Singh, Hydrodynamics of fluidization using kinetic theory: An emerging paradigm, *Powder Technol.* 148 (2−3) (2004) 123−141.
[49] S.E. Harris, D.G. Crighton, Solitons, solitary waves, and voidage disturbances in gas-fluidized beds, *J. Fluid Mech.* 266 (1994) 243−276.
[50] F.M. Auzerais, R. Jackson, W.B. Russel, The resolution of shocks and the effects of compressible sediments in transient settling, *J. Fluid Mech.* 195 (1988) 437−462.
[51] Y. Wu, D.Y. Liu, J.D. Hu, J.L. Ma, X.P. Chen, Comparative study of two fluid model and dense discrete phase model for simulations of gas−solid hydrodynamics in circulating fluidized beds, *Particuology* 55 (2021) 108−117.
[52] A. Nikolopoulos, A. Stroh, M. Zeneli, F. Alobaid, N. Nikolopoulos, J. Ströhle, S. Karellas, B. Epple, P. Grammelis, Numerical investigation and comparison of coarse grain CFD-DEM and TFM in the case of a 1 MW_{th} fluidized bed carbonator simulation, *Chem. Eng. Sci.* 163 (2017) 189−205.
[53] P. Ostermeier, S. DeYoung, A. Vandersickel, S. Gleis, H. Spliethoff, Comprehensive investigation and comparison of TFM, DenseDPM and CFD-DEM for dense fluidized beds, *Chem. Eng. Sci.* 196 (2019) 291−309.
[54] J.L. Song, D.Y. Liu, J.L. Ma, X.P. Chen, Effect of elevated pressure on bubble properties in a two-dimensional gas−solid fluidized bed, *Chem. Eng. Res. Des.* 138 (2018) 21−31.
[55] D.Y. Liu, X.P. Chen, Lateral solids dispersion coefficient in large-scale fluidized beds, *Combust. Flame* 157 (11) (2010) 2116−2124.
[56] D. Bai, E. Shibuya, Y. Masuda, K. Nishio, N. Nakagawa, K. Kato, Distinction between upward and downward flows in circulating fluidized beds, *Powder Technol.* 84 (1) (1995) 75−81.
[57] J.R. Grace, High-velocity fluidized bed reactors, *Chem. Eng. Sci.* 45 (8) (1990) 1953−1966.
[58] S. Mahmoudi, C.W. Chan, A. Brems, J. Seville, J. Baeyens, Solids flow diagram of a CFB riser using Geldart B-type powders, *Particuology* 10 (1) (2012) 51−61.